

See discussions, stats, and author profiles for this publication at: <https://www.researchgate.net/publication/268795674>

# Controllable Synthesis of Ordered Mesoporous NiFe<sub>2</sub>O<sub>4</sub> with Tunable Pore Structure as a Bifunctional Catalyst for Li–O<sub>2</sub> Batteries

ARTICLE in ACS APPLIED MATERIALS & INTERFACES · NOVEMBER 2014

Impact Factor: 6.72 · DOI: 10.1021/am505718k · Source: PubMed

---

CITATIONS

5

---

READS

98

## 7 AUTHORS, INCLUDING:



Kun Guo

University of Stavanger (UiS)

6 PUBLICATIONS 54 CITATIONS

[SEE PROFILE](#)

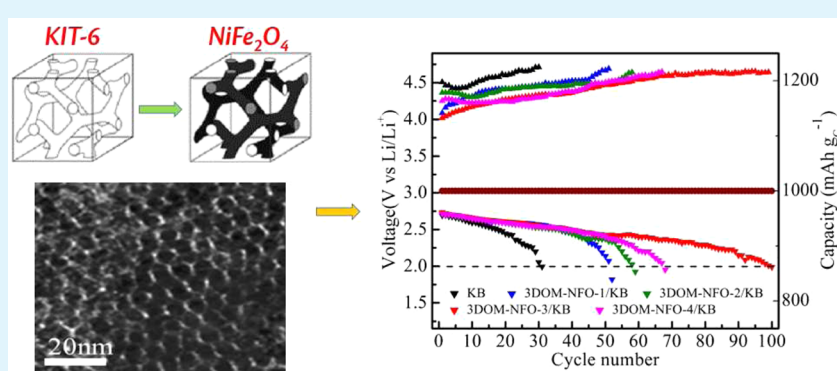
# Controllable Synthesis of Ordered Mesoporous $\text{NiFe}_2\text{O}_4$ with Tunable Pore Structure as a Bifunctional Catalyst for $\text{Li}-\text{O}_2$ Batteries

Yuan Li,<sup>†,‡</sup> Kun Guo,<sup>†</sup> Jun Li,<sup>†</sup> Xiaowen Dong,<sup>†</sup> Ting Yuan,<sup>\*,†</sup> Xiaowei Li,<sup>§</sup> and Hui Yang<sup>\*,†</sup>

<sup>†</sup>Shanghai Advanced Research Institute, Chinese Academy of Sciences, Shanghai 201210, China

<sup>‡</sup>Technology Center, China Tobacco Hebei Industrial Company, Ltd., Shijiazhuang 050051, China

<sup>§</sup>College of Physics, Optoelectronics and Energy of Soochow University, Suzhou 215123, China



**ABSTRACT:** Three-dimensional ordered mesoporous (3DOM)  $\text{NiFe}_2\text{O}_4$  materials with tunable pore size ranging from 5.0 to 25.1 nm have been synthesized via a hard template and used as bifunctional electrocatalysts for rechargeable  $\text{Li}-\text{O}_2$  batteries. Characterization of the catalysts by X-ray diffraction and transmission electron microscopy confirms the formation of a single-phase 3DOM  $\text{NiFe}_2\text{O}_4$  structure. Linear scanning voltammetry measurements reveal that Ketjen black (KB) carbon-supported 3DOM  $\text{NiFe}_2\text{O}_4$  exhibits a decreased overpotential for both oxygen reduction reaction (ORR) and oxygen evolution reaction (OER) than commonly used KB. A reduction in both the ORR and OER overpotentials increases with the mean pore size of 3DOM  $\text{NiFe}_2\text{O}_4$  materials. Importantly,  $\text{Li}-\text{O}_2$  batteries with 3DOM  $\text{NiFe}_2\text{O}_4$  materials as the cathode catalysts exhibit a significant enhancement in the discharge capacity, rate capability, and cyclability, and these performances increases with the mean pore size of 3DOM  $\text{NiFe}_2\text{O}_4$  materials. For a  $\text{Li}-\text{O}_2$  battery equipped with a 3DOM  $\text{NiFe}_2\text{O}_4$  catalyst with a maximum mean pore size of 25.1 nm, a long cycling life of up to 100 cycles under the limiting capacity of  $1000 \text{ mAh g}_\text{C}^{-1}$  is achieved, strongly indicating that the mesoporous size of the bifunctional catalysts plays a crucial role in enhancing the performance of  $\text{Li}-\text{O}_2$  batteries. The combined use of 3DOM  $\text{NiFe}_2\text{O}_4$  with a maximal pore size of 25.1 nm and a poly(vinylidene difluoride hexafluoropropylene) separator with a tuned pore structure further improves the  $\text{Li}-\text{O}_2$  battery performance, highlighting the importance of the pore structure in the development of bifunctional catalysts and separators.

**KEYWORDS:** lithium–oxygen batteries, tunable pore size, ordered mesoporous structure, nickel ferrite, bifunctional electrocatalysts

## 1. INTRODUCTION

Nonaqueous lithium–oxygen ( $\text{Li}-\text{O}_2$ ) secondary batteries based on the reversible formation and decomposition of insoluble lithium peroxide ( $\text{Li}_2\text{O}_2$ ) have received much attention owing to their potential to provide an ultrahigh theoretical energy density. However, the performance of the present  $\text{Li}-\text{O}_2$  batteries is far from the expected applications, mainly because of (i) the chemical instability of aprotic solvents and prevailing carbon electrodes<sup>1–7</sup> and (ii) the intrinsic sluggish kinetics of the oxygen reduction reaction (ORR) and oxygen evolution reaction (OER).<sup>3,5,8–10</sup> Thus, the search for highly active electrocatalysts with optimized structures to address the inherent problems associated with the present  $\text{Li}-\text{O}_2$  batteries is very crucial.

Extensive research has been directed toward the development of high-performance bifunctional electrocatalysts with

various structures and morphologies. Among them, porous materials have been widely applied and testified to improve the performance of  $\text{Li}-\text{O}_2$  batteries owing to their favorable frameworks with high surface areas and large pore volumes. To date, carbon materials with various pore sizes,<sup>11–13</sup> mesoporous  $\text{TiN}$ ,<sup>14</sup> porous  $\text{Co}_3\text{O}_4$ ,<sup>15,16</sup> mesoporous  $\text{NiCo}_2\text{O}_4$  nanoflakes,<sup>17</sup> porous  $\text{La}_{0.75}\text{Sr}_{0.25}\text{MnO}_3$  nanotubes,<sup>18</sup> etc., have been successfully incorporated to reduce the discharge–charge overpotentials, thus improving the specific capacity and rate capability and extending the cycle life of the  $\text{Li}-\text{O}_2$  batteries. Such porous structural features offer the benefits of massive channels for rapid oxygen diffusion, sufficient reactive sites for

Received: August 24, 2014

Accepted: November 18, 2014

Published: November 18, 2014



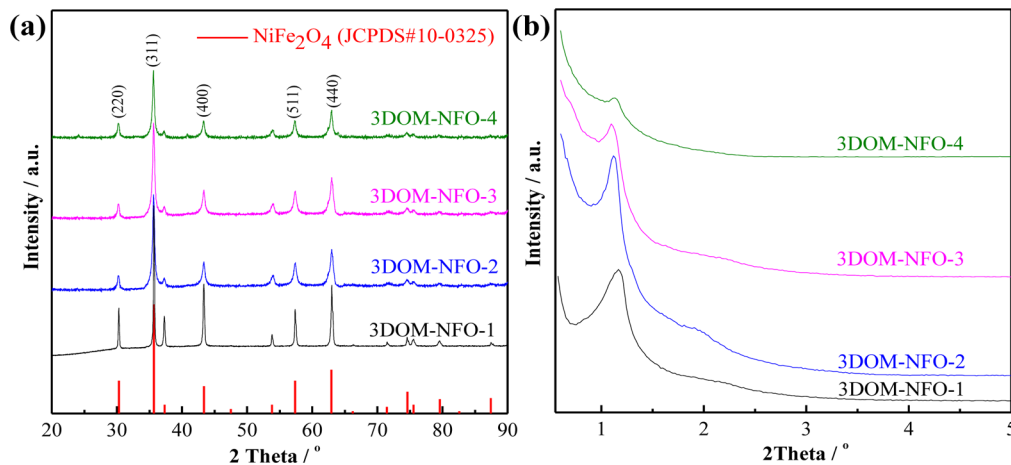


**Figure 1.** Wide- (a) and small-angle (b) XRD patterns of the 3DOM  $\text{NiFe}_2\text{O}_4$  samples.

$\text{Li}-\text{O}_2$  reactions, and a large storage space for  $\text{Li}_2\text{O}_2$  deposition upon discharge. More recently, Zhang et al.<sup>19</sup> reported that the use of three-dimensional (3D) macroporous  $\text{LaFeO}_3$  nanoparticles as electrocatalysts for  $\text{Li}-\text{O}_2$  batteries results in an enhanced performance, indicating the importance of the porous structure. However, the correlation between the pore sizes, in particular, with a narrow distribution and catalytic activity of the mesoporous catalysts has rarely been reported. Early reports<sup>20,21</sup> have partially demonstrated that the pore size instead of the surface area of carbon materials might play a key role in determining the discharge capacity of  $\text{Li}-\text{O}_2$  batteries. Moreover, most of the reported mesoporous catalysts are synthesized with a broad pore-size distribution and nonordered structure, making it complicated to investigate the effect of the pore size/structure on the performance of the catalysts. Thus, the synthesis of highly ordered mesoporous electrocatalysts with controllable pore size to investigate the optimized structure for enhancing the round-trip efficiency, rate capability, and cyclability of  $\text{Li}-\text{O}_2$  batteries still remains a big challenge.

Recently, spinel-type metal oxides have emerged as a promising electrode material for supercapacitors,<sup>22–24</sup> lithium-ion batteries,<sup>25–27</sup> and metal-air batteries.<sup>28–30</sup>  $\text{NiFe}_2\text{O}_4$ , as one of the spinel ferrites, might exhibit an enhanced catalytic activity toward both the ORR and OER because of the presence of multivalence elements  $\text{Ni}^{3+}/\text{Ni}^{2+}$  and  $\text{Fe}^{3+}/\text{Fe}^{2+}$ . Compared to the reported Co- or Mn-based spinels, Fe- and Ni-containing  $\text{NiFe}_2\text{O}_4$  is inexpensive, abundant, and environmentally benign for potential applications.<sup>31–33</sup> These benefits enable  $\text{NiFe}_2\text{O}_4$  to be a promising candidate as electrocatalysts for  $\text{Li}-\text{O}_2$  batteries. Herein, we report a controllable synthesis of a 3D-ordered mesoporous (3DOM)  $\text{NiFe}_2\text{O}_4$  with a tunable pore size using KIT-6 as the hard template. The 3DOM  $\text{NiFe}_2\text{O}_4$  materials with different pore sizes are further utilized as bifunctional catalysts to explore the effect of the mesopore size on the  $\text{Li}-\text{O}_2$  battery performance. The specific capacity, rate capability, and cyclability are all enhanced proportionally to the pore size of 3DOM  $\text{NiFe}_2\text{O}_4$ . Furthermore, on the basis of the previous report on fast  $\text{Li}^+$  transfer within a separator with tuned pore structure,<sup>34</sup> it would be interesting to combine both optimized materials in  $\text{Li}-\text{O}_2$  batteries. The performance is testified experimentally for further improvement by combining the 3DOM  $\text{NiFe}_2\text{O}_4$  electrocatalyst with a poly(vinylidene difluoride hexafluoropropylene) (PVdF-HFP) separator. This enhancement, which is closely related to the pore structure of

both 3DOM  $\text{NiFe}_2\text{O}_4$  and a PVdF-HFP separator, would provide valuable insight for the future development of key porous materials for  $\text{Li}-\text{O}_2$  batteries.

## 2. EXPERIMENTAL SECTION

**2.1. Preparation of the KIT-6 Template.** KIT-6, with  $I\bar{a}3d$  symmetry containing 3D bicontinuous mesochannel networks, is one of the commonly used mesoporous silica templates. Highly ordered mesoporous KIT-6 templates were synthesized according to the previously reported procedures.<sup>35,36</sup> By adjustment of the acidity of the solution from 0.5 to 1.5 M HCl and the hydrothermal reaction temperature (i.e., aging temperature) in the range of 40–130 °C, KIT-6 templates with different pore structures were obtained<sup>37</sup> and abbreviated as KIT-6-1, KIT-6-2, KIT-6-3, and KIT-6-4 with decreasing aging temperature.

**2.2. Synthesis of 3DOM  $\text{NiFe}_2\text{O}_4$ .** Mesoporous  $\text{NiFe}_2\text{O}_4$  materials were synthesized as follows. A KIT-6 mesoporous silica template (0.3 g) was impregnated with 1 mmol of  $\text{Ni}(\text{NO}_3)_2 \cdot 6\text{H}_2\text{O}$  and 2 mmol of  $\text{Fe}(\text{NO}_3)_2 \cdot 6\text{H}_2\text{O}$  dissolved in 0.5 mL of ethanol and stirred at room temperature until ethanol was completely volatilized; the sample was then heated slowly to 300 °C and calcined at the same temperature for 2 h to pyrolyze the nitrate. The impregnation procedure was repeated twice with 0.6 and 0.3 times the amounts for  $\text{Ni}(\text{NO}_3)_2 \cdot 6\text{H}_2\text{O}$  and  $\text{Fe}(\text{NO}_3)_2 \cdot 6\text{H}_2\text{O}$ , respectively, and then the samples were calcined at 550 °C for 5 h in a muffle under an air atmosphere for crystallization of the metal oxide. Subsequently, the silica matrix was removed with a 2 M NaOH solution at 60 °C for 24 h under magnetic stirring. Finally, the product was filtered and washed with water and ethanol several times and dried under vacuum at 80 °C for more than 4 h. The products corresponding to different KIT-6 templates were labeled as 3DOM-NFO-1, 3DOM-NFO-2, 3DOM-NFO-3, and 3DOM-NFO-4.

**2.3. Preparation of PVdF-HFP Membranes with Tuned Pore Structures.** PVdF-HFP membranes with tuned pore structures were prepared as previously reported<sup>34</sup> and used as separators for  $\text{Li}-\text{O}_2$  batteries.

**2.4. Structural Characterization.** The structure, morphology, and pore-size distribution of the as-prepared 3DOM  $\text{NiFe}_2\text{O}_4$  nanoparticles were examined by X-ray diffraction (XRD; Bruker D8 Advance), scanning electron microscopy (SEM; Hitachi S-4800), transmission electron microscopy (TEM; JEOL JEM 200), and Brunauer–Emmett–Teller (BET) analysis (ASAP 2020). For XRD and SEM analysis of the cycled electrodes, the electrodes were placed in an argon-filled glovebox to avoid exposure to the ambient atmosphere.

**2.5.  $\text{Li}-\text{O}_2$  Battery Assembly and Performance Measurements.** According to our previous work,<sup>38</sup> the air electrode was prepared as follows. Typically, an ink slurry was prepared by dispersing 45 wt % as-prepared 3DOM  $\text{NiFe}_2\text{O}_4$ , 45 wt % Ketjen black EC600JD

(KB; 90 wt % KB for a bare KB electrode), and 10 wt % poly(tetrafluoroethylene) as the binder in isopropyl alcohol and dispersed by mechanical stirring and sonication. Then, the ink slurry was spread layer-by-layer by hand-painting on the carbon paper (TGP-H-060, E-TEK Inc.) with a loading of  $2.0 \pm 0.2 \text{ mg cm}^{-2}$  and on the bare KB electrode with a loading of  $1.0\text{--}1.2 \text{ mg cm}^{-2}$ . Then, the air electrodes were dried under vacuum at  $60^\circ\text{C}$  for 12 h. The PP/PE/PP (Celgard 2325; PP = polypropylene and PE = polyethylene) and glass fiber (Whatman) separators or PVdF-HFP separators were soaked in 1 M  $\text{LiCF}_3\text{SO}_3$ -TEGDEM electrolyte. Metallic lithium foil with a thickness of 0.50 mm was used as the anode. A Swagelok cell with an air hole of 10 mm diameter was used. The cell was assembled in an argon-filled glovebox and tested in an oxygen-filled bottle at an oxygen pressure of  $\sim 1$  atm. Linear scanning voltammetry (LSV) was conducted in a three-electrode electrochemical cell on a CHI 730B electrochemical workstation. The aforesaid oxygen electrode was used as the working electrode, and lithium metal foils were used as the counter and reference electrodes. Prior to each experiment, the electrolyte solutions were purged with  $\text{O}_2$  or  $\text{N}_2$  for at least 20 min. The galvanostatic discharge–charge performance was evaluated using the LAND test system (Wuhan Land Electronic Co. Ltd, China) within the voltage range of 2.0–4.5 V. The capacity was normalized to the mass of KB. For the cyclability test, the discharge–charge capacity is restricted to  $1000 \text{ mAh g}_\text{C}^{-1}$ , and the test will stop when the terminal discharge voltage falls below 2.0 V.

### 3. RESULTS AND DISCUSSION

Figure 1 shows the wide- and small-angle XRD patterns of the as-prepared  $\text{NiFe}_2\text{O}_4$  catalysts. The results are consistent with the spinel crystalline structure  $\text{NiFe}_2\text{O}_4$  (JCPDF 10-0325). The distinct peaks in the wide-angle XRD pattern were observed at  $2\theta$  values of  $30.29$ ,  $35.69$ ,  $43.36$ ,  $57.36$ , and  $62.92^\circ$  corresponding to  $(220)$ ,  $(311)$ ,  $(400)$ ,  $(511)$ , and  $(440)$  plane reflections of the spinel  $\text{NiFe}_2\text{O}_4$  structure, respectively. The small-angle XRD patterns showed the well-resolved diffraction peak at  $2\theta$  of  $\sim 1.1\text{--}1.2^\circ$  associated with the  $(211)$  reflection, showing that the pore symmetry of cubic  $I\bar{a}3d$  was successfully replicated.

The morphology and pore structure of the  $\text{NiFe}_2\text{O}_4$  samples were further characterized by TEM and high-resolution TEM (HRTEM). Parts a–d of Figure 2 show the representative TEM images of  $\text{NiFe}_2\text{O}_4$  obtained from the replication of 3D cubic  $I\bar{a}3d$  KIT-6 silica templates. All of the samples show a regular-ranged channel, and the pore sizes of the  $\text{NiFe}_2\text{O}_4$  samples gradually increase, as shown in Figure 2a–d. In the HRTEM images (Figure 2e,f), two types of lattice fringes are clearly observed, and the spacing distances between adjacent fringes are  $0.251$  and  $0.213 \text{ nm}$ , which are in conformity with the  $(311)$  and  $(220)$  lattice spacing distances of spinel  $\text{NiFe}_2\text{O}_4$ , respectively. These results further prove that the as-prepared samples are spinel-structured 3DOM  $\text{NiFe}_2\text{O}_4$  materials.

Figure 3 shows the  $\text{N}_2$  adsorption–desorption isotherm and pore-size distribution of 3DOM  $\text{NiFe}_2\text{O}_4$  materials. The isotherms of the mesostructured  $\text{NiFe}_2\text{O}_4$  samples are of type IV, and all of them exhibit a H3 hysteresis loop, indicative of the presence of mesopores. However, the hysteresis loop of the 3DOM-NFO-4 sample is not as clear as the other samples, suggesting that the 3DOM-NFO-4 sample contains a certain amount of nonmesopores. The pore-size distributions of the 3DOM  $\text{NiFe}_2\text{O}_4$  samples are shown in Figure 3b. Both the 3DOM-NFO-1 and 3DOM-NFO-2 samples exhibit narrow pore-size distributions mainly concentrated in the sizes of  $4.8$  and  $7.7 \text{ nm}$ , respectively, demonstrating that the samples well replicate the pore structure of the KIT-6 template. 3DOM-NFO-3 and 3DOM-NFO-4 show wide pore-size distributions,

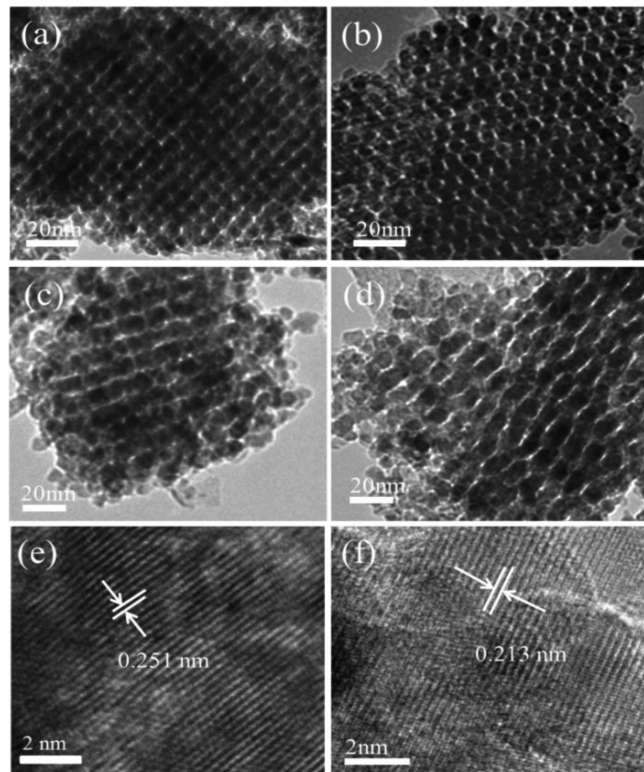


**Figure 2.** TEM (a–d) and HRTEM (e and f) images of 3DOM  $\text{NiFe}_2\text{O}_4$  with varying pore sizes.

probably because of the partly replicating single set of the helix channel instead of the double-helix structure and/or because the precursor solution failed to be adsorbed completely into the pores of the template. A further increase in the pore size to a larger size while replicating the cubic  $I\bar{a}3d$  structure is very difficult. The specific surface area, pore size, and pore volume data are listed in Table 1. The specific surface areas are in the range of  $89\text{--}124 \text{ m}^2 \text{ g}^{-1}$  and are uncorrelated with the pore size, which could be attributed to the broad distributions of the pore sizes of the 3DOM-NFO-3 and 3DOM-NFO-4 samples, while the pore volume increases with the pore size.

Figure 4 is a comparison of the LSV curves of the ORR in an  $\text{O}_2$ -saturated electrolyte and of the OER in an  $\text{N}_2$ -saturated electrolyte on both the 3DOM  $\text{NiFe}_2\text{O}_4$ /KB and KB electrodes. For the ORR (Figure 4a), the onset potential is higher than the standard potential for the formation of  $\text{Li}_2\text{O}_2$  ( $2.96 \text{ V}_\text{Li}$ ), indicating that the reduction current is partly contributed by some side reactions induced by the presence of a catalyst and  $\text{O}_2$ . Nevertheless, the 3DOM  $\text{NiFe}_2\text{O}_4$ /KB electrodes exhibit more positive ORR potentials and higher current densities than the KB electrode. More importantly, the ORR activity on 3DOM  $\text{NiFe}_2\text{O}_4$  gradually increases with its pore size, which should be attributed to more active sites and the large pore volume of the 3DOM-NFO-4 sample. Because the OER refers to the decomposition of lithium oxides, the tests of the OER activity on the 3DOM  $\text{NiFe}_2\text{O}_4$ /KB and KB electrodes were conducted by depositing lithium oxides onto the surface through discharge of these electrodes to  $2500 \text{ mAh g}_\text{C}^{-1}$  before the LSV test.<sup>18</sup> The OER polarization curves in Figure 4b also indicate higher OER current density and more negative OER potential for the 3DOM  $\text{NiFe}_2\text{O}_4$ /KB electrode than for the KB electrode, demonstrating that 3DOM  $\text{NiFe}_2\text{O}_4$  electrocatalysts also showed good OER catalytic activity. The

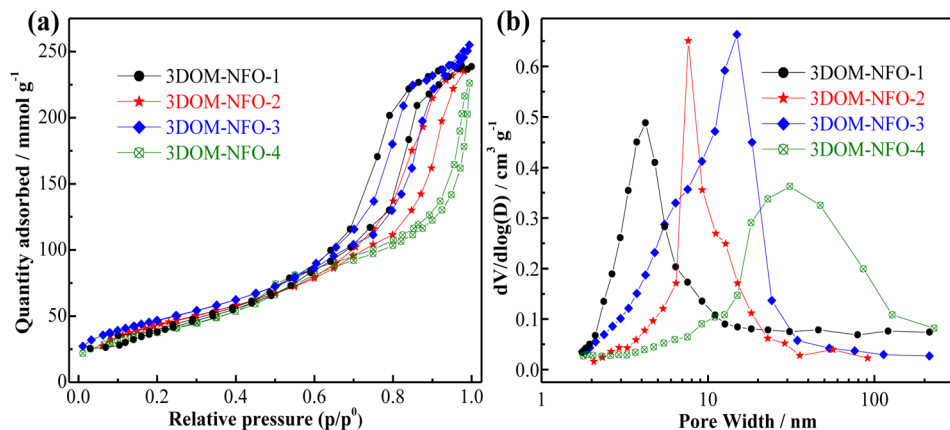


**Figure 3.** N<sub>2</sub> adsorption–desorption isotherms (a) and pore-size distributions (b) of the 3DOM NiFe<sub>2</sub>O<sub>4</sub> sample with different pore sizes.

**Table 1. BET Specific Area and Pore Structural Properties of 3DOM NiFe<sub>2</sub>O<sub>4</sub> Samples with Different Pore Sizes**

sample	specific area/m <sup>2</sup> g <sup>-1</sup>	mean pore diameter/nm	pore volume/cm <sup>3</sup> g <sup>-1</sup>
3DOM-NFO-1	89.8	5.0	0.13
3DOM-NFO-2	107.5	7.9	0.23
3DOM-NFO-3	123.4	12.8	0.32
3DOM-NFO-4	105.2	25.1	0.36

OER catalytic activity increases with the pore size and pore volume, probably because of the improvement of the utilizing ratio of the pore volume with larger pore size. Although the specific mechanism about the catalytic process is still unclear, the LSV results definitely prove that the 3DOM NiFe<sub>2</sub>O<sub>4</sub> electrode shows excellent ORR and OER bifunctional catalytic activity, which increases with the pore size of the 3DOM NiFe<sub>2</sub>O<sub>4</sub> catalyst, thus reducing the overpotential and improving the charge–discharge efficiency of Li–O<sub>2</sub> batteries.

Figure 5a depicts the first discharge–charge curves of Li–O<sub>2</sub> batteries with 3DOM NiFe<sub>2</sub>O<sub>4</sub> catalysts of different pore sizes at a current density of 0.1 mA cm<sup>-2</sup>. The specific capacity of Li–O<sub>2</sub> batteries with 3DOM NiFe<sub>2</sub>O<sub>4</sub> catalysts, especially the 3DOM-NFO-4 sample, are all above 10000 mAh g<sub>C</sub><sup>-1</sup>, which is much higher than 4454 mAh g<sub>C</sub><sup>-1</sup> of the KB electrode. The discharge voltage plateaus show a similar variation trend and are 50–120 mV higher than that with the KB electrode. In addition, all of the recharge plateaus are much lower than that

of the KB electrode (~4.10 V) and even decrease from 3.97 to 3.60 V when using the 3DOM-NFO-4 catalyst, which is comparable with the reported catalysts.<sup>18,19</sup> The round-trip efficiencies of Li–O<sub>2</sub> batteries increase with the pore size of 3DOM NiFe<sub>2</sub>O<sub>4</sub> from 68.7% to 71.8%, which are higher than that with KB with a round-trip efficiency of 61.1%. These results indicate that the existence of 3DOM NiFe<sub>2</sub>O<sub>4</sub> can effectively reduce the cathodic polarization and thus improve the round-trip efficiency of Li–O<sub>2</sub> batteries, which should be attributed to the synergistic effect of the inherent catalytic activity of spinel-type NiFe<sub>2</sub>O<sub>4</sub> and its 3DOM structure. The 3DOM structure is conducive to the transport of a Li<sup>+</sup> ion and an O<sub>2</sub> molecule through the channels during the reaction process, and the large pore volume provides accommodation for Li<sub>2</sub>O<sub>2</sub> deposition inside the channels instead of on the surface of the electrode.<sup>20,21</sup> These advantages are more obviously presented in 3DOM NiFe<sub>2</sub>O<sub>4</sub> with a larger pore size, which explains the gradually enhanced performance of Li–O<sub>2</sub> batteries with increasing pore size and pore volume of 3DOM NiFe<sub>2</sub>O<sub>4</sub> catalysts.

Parts b–d of Figure 5 show the first discharge–charge behavior of Li–O<sub>2</sub> batteries with different 3DOM NiFe<sub>2</sub>O<sub>4</sub>/KB and KB catalysts at current densities of 0.2, 0.5, and 1 mA cm<sup>-2</sup>, respectively. It can be observed that the discharge–charge overpotentials increase and the specific capacities decrease at a higher current density. However, the battery with the 3DOM NiFe<sub>2</sub>O<sub>4</sub>/KB catalyst exhibits a much better rate capability than

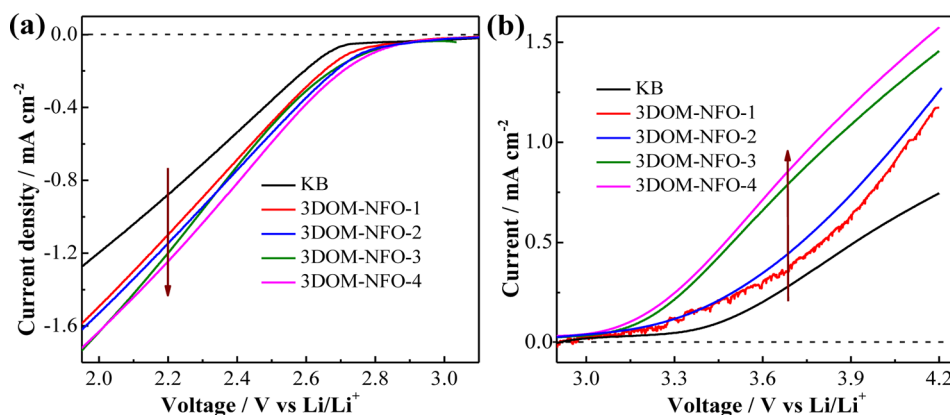


**Figure 4.** LSV curves of the ORR (a) and OER (b) for electrodes with 3DOM NiFe<sub>2</sub>O<sub>4</sub> of different pore sizes and KB in 1 M LiCF<sub>3</sub>SO<sub>3</sub>–TEGDME electrolytes at a scan rate of 10 mV s<sup>-1</sup>.

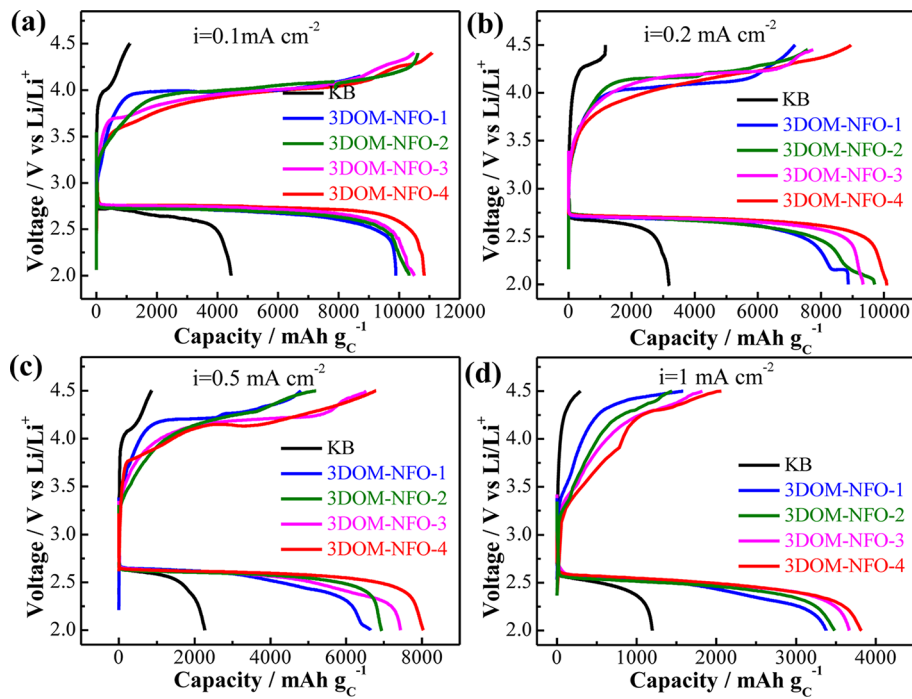


**Figure 5.** Discharge–charge curves at  $0.1 \text{ mA cm}^{-2}$  (a),  $0.2 \text{ mA cm}^{-2}$  (b),  $0.5 \text{ mA cm}^{-2}$  (c), and  $1 \text{ mA cm}^{-2}$  (d) of the  $\text{Li}-\text{O}_2$  batteries with different pore sizes of 3DOM  $\text{NiFe}_2\text{O}_4$  and KB as the catalysts.

that with pure KB. Importantly, 3DOM-NFO-4 electrodes, equipped with the largest pore size and pore volume, show the best performance, and the first specific discharge capacities at  $0.2$ ,  $0.5$ , and  $1 \text{ mA cm}^{-2}$  reach  $10084$ ,  $8038$ , and  $3808 \text{ mAh g}_C^{-1}$ , respectively, and are higher than  $3190$ ,  $2270$ , and  $1316 \text{ mAh g}_C^{-1}$  for the KB electrodes. Table 2 lists the rate capability

$\text{Li}_2\text{O}_2$  film,<sup>39</sup> which could not enter the mesopores, thus evidently reducing the utilization rate of the pore volume.

Figure 6 shows the discharge–charge profiles at different cycles of the  $\text{Li}-\text{O}_2$  batteries with different catalysts and terminal voltage profiles with a capacity restriction of  $1000 \text{ mAh g}_C^{-1}$  at  $0.1 \text{ mA cm}^{-2}$ . As seen in Figure 6a–e, the  $\text{Li}-\text{O}_2$  batteries with 3DOM  $\text{NiFe}_2\text{O}_4$  catalysts obtain a much lower charge voltage plateau, which could reduce decomposition of the electrolyte and corrosion of the carbon materials. Although a decrease in the cutoff voltage is observed during the cycling, the battery with the 3DOM  $\text{NiFe}_2\text{O}_4/\text{KB}$  electrode exhibits better cyclability, and the cycle life extends to 100 cycles with increasing pore size. In contrast, the operations of the  $\text{Li}-\text{O}_2$  batteries with the KB electrode are limited to only 12 cycles (Figure 6a). These results highlight the power of the 3DOM  $\text{NiFe}_2\text{O}_4$  electrocatalyst and indicate that the pore size may be an important factor for the performance of  $\text{Li}-\text{O}_2$  batteries.

Figure 7 shows the XRD patterns of the electrodes with the KB and 3DOM-NFO-3/KB catalysts in  $\text{Li}-\text{O}_2$  batteries before and after discharge and after recharge. Apart from the diffraction peaks of  $\text{NiFe}_2\text{O}_4$  and carbon paper, the XRD patterns of the discharged and recharged electrodes are compared to the initial one to check the appearance of any new peaks. In Figure 7a, after the discharge, the peaks indexed to  $\text{Li}_2\text{O}_2$  clearly appear on the electrode with the KB catalyst, while after the recharge, the peaks do not completely disappear, indicating that  $\text{Li}_2\text{O}_2$  still remains, explaining the short duration of the charge process, as shown in Figure 4. In Figure 7b,  $\text{Li}_2\text{O}_2$  phases are formed after the discharge, whereas after the recharge, both of them disappear. These results are consistent with the high OER catalytic activity of  $\text{Li}-\text{O}_2$  batteries with the 3DOM  $\text{NiFe}_2\text{O}_4$  catalyst.

For further insights of discharge and charge processes of  $\text{Li}-\text{O}_2$  batteries with the KB and 3DOM-NFO/KB catalysts, a field-emission SEM technique was employed to analyze the surface morphology (Figure 8) at different discharge–charge

**Table 2. Rate Performance of  $\text{Li}-\text{O}_2$  Batteries with Different Catalysts**

catalyst	specific capacity at $0.1 \text{ mA cm}^{-2}/\text{mAh g}_C^{-1}$	capacity retention rate/%		
		$0.2 \text{ mA cm}^{-2}$	$0.5 \text{ mA cm}^{-2}$	$1 \text{ mA cm}^{-2}$
3DOM-NFO-1/ KB	9892	89.7	62.7	34.1
3DOM-NFO-2/ KB	10486	90.2	67.5	33.7
3DOM-NFO-3/ KB	10620	92.1	71.4	34.9
3DOM-NFO-4/ KB	10830	93.0	74.7	35.2
KB	4454	71.5	50.9	26.8

of  $\text{Li}-\text{O}_2$  batteries with 3DOM  $\text{NiFe}_2\text{O}_4/\text{KB}$  and pure KB. The capacity retention rate refers to the ratio of the discharge capacity at the corresponding current density and that at  $0.1 \text{ mA cm}^{-2}$ . The results indicate that the rate capability of  $\text{Li}-\text{O}_2$  batteries was enhanced by the 3DOM  $\text{NiFe}_2\text{O}_4$  catalyst and increased with the pore size of the catalyst, ascribing good bifunctional catalytic activity, as proven by the LSV results and 3DOM structure conducive to the  $\text{Li}^+$  and  $\text{O}_2$  transform. However, the effect of the catalyst pore size on the battery performance reduces with increasing current density. When discharged at a high rate, the discharge products formed a thin

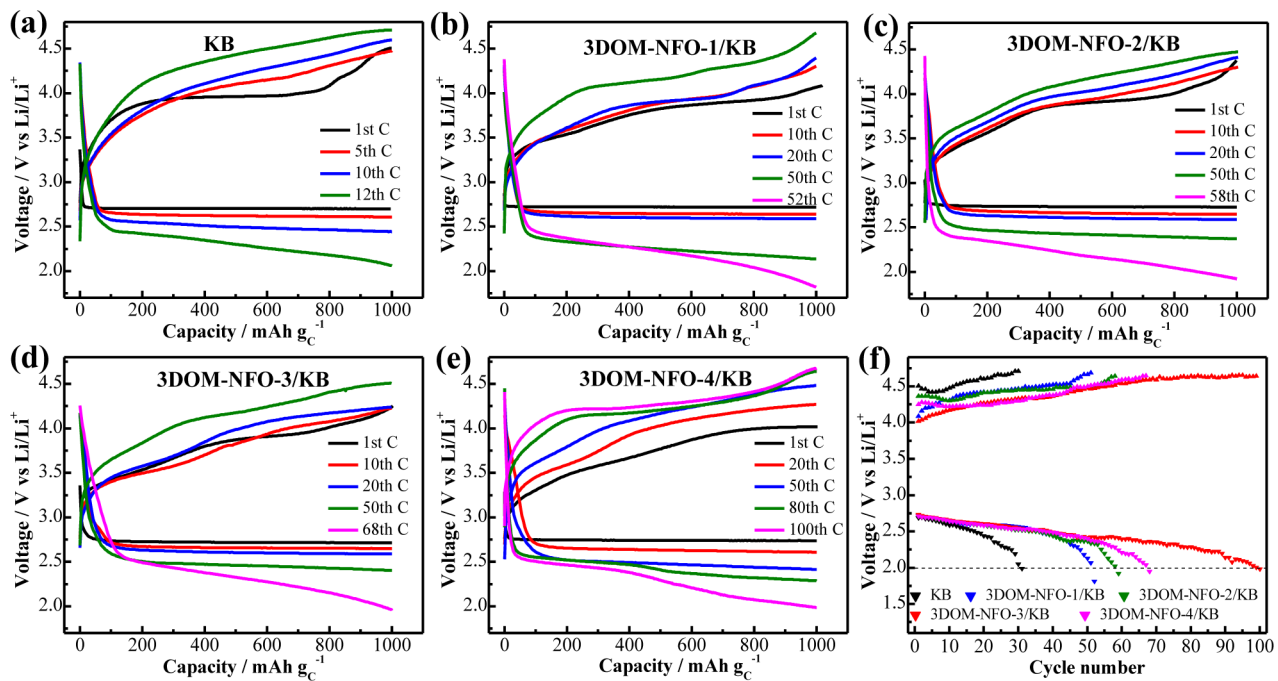


**Figure 6.** Discharge–charge profiles at different cycles of the Li–O<sub>2</sub> batteries with KB (a), 3DOM-NFO-1/KB (b), 3DOM-NFO-2/KB (c), 3DOM-NFO-3/KB (d), and 3DOM-NFO-4/KB catalysts (e) and terminal voltage profiles (f) with a capacity restriction of 1000 mAh g<sub>C</sub><sup>-1</sup> at 0.1 mA cm<sup>-2</sup>.

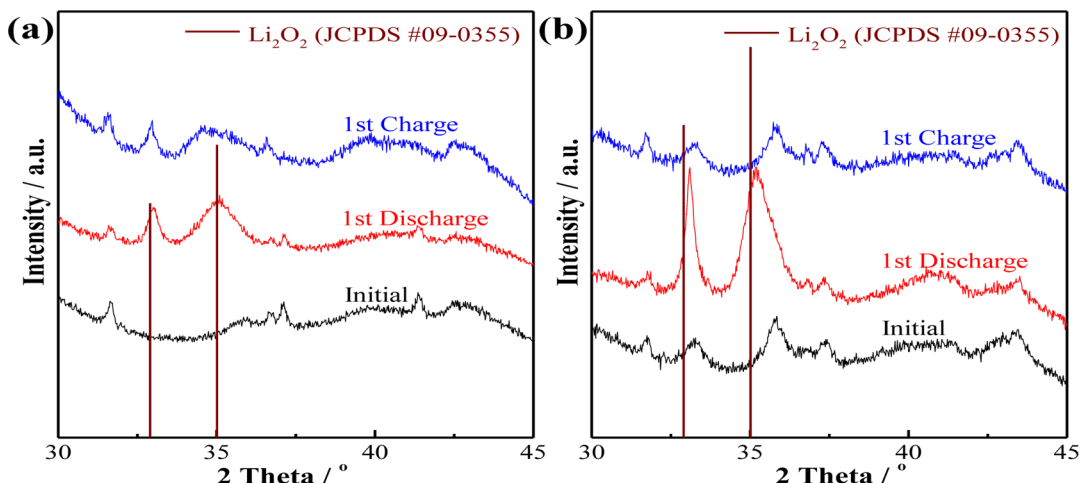


**Figure 7.** XRD patterns of the cathodes with KB (a) and 3DOM-NFO-3/KB (b) catalysts at different discharge–charge stages.

stages. Figure 8a depicts the initial morphology of the 3DOM-NFO-3/KB electrode. Microspheres are observed on the surface of the electrode because of the aggregation of 3DOM NiFe<sub>2</sub>O<sub>4</sub> and KB. After the discharge, the microspheres are covered by massive toroidal-shaped blocks, as shown in Figure 8b. On the basis of the previous reports,<sup>39–41</sup> the toroidal-shaped blocks are Li<sub>2</sub>O<sub>2</sub>; therefore, blocking the pathways for oxygen diffusion and electron transfer leads to discharge termination. The morphological change in the 3DOM-NFO-3/KB electrodes after the subsequent recharge is shown in Figure 8c. The toroidal-shaped Li<sub>2</sub>O<sub>2</sub> disappears, and the surface returns back to the structure with microspheres. After 10 cycles, the electrode surface still shows the microsphere morphology but the size increases slightly (Figure 8d), manifesting that 3DOM NiFe<sub>2</sub>O<sub>4</sub> facilitates decomposition of the discharge products but cannot decompose completely, thus leading to an incompletely recovered morphology after long cycling time.

This might be because of two aspects: Li<sub>2</sub>O<sub>2</sub> cannot decompose completely by the 3DOM NiFe<sub>2</sub>O<sub>4</sub> catalyst during charging and/or accumulation of the irreversible electrolyte decomposition product formed on the surface.

The above results demonstrate the enhanced performance of Li–O<sub>2</sub> batteries with increasing pore size of the 3DOM NiFe<sub>2</sub>O<sub>4</sub> catalysts. According to the previous report,<sup>34</sup> the pore structure of the separator also plays an important role in improving the rate capability. It has been proven that the PVdF-HFP separator with a tuned pore structure exhibits an optimized Li<sup>+</sup> transport, which enhances the rate capability of Li–O<sub>2</sub> batteries. To further verify the effect of the pore structure on the battery performance, we then extended the battery test by combining the 3DOM-NFO-4 catalyst and previously optimized PVdF-HFP separator. The discharge curves of the Li–O<sub>2</sub> batteries with these materials at 1 and 5 mA cm<sup>-2</sup> are shown in Figure 9. The discharge specific capacity

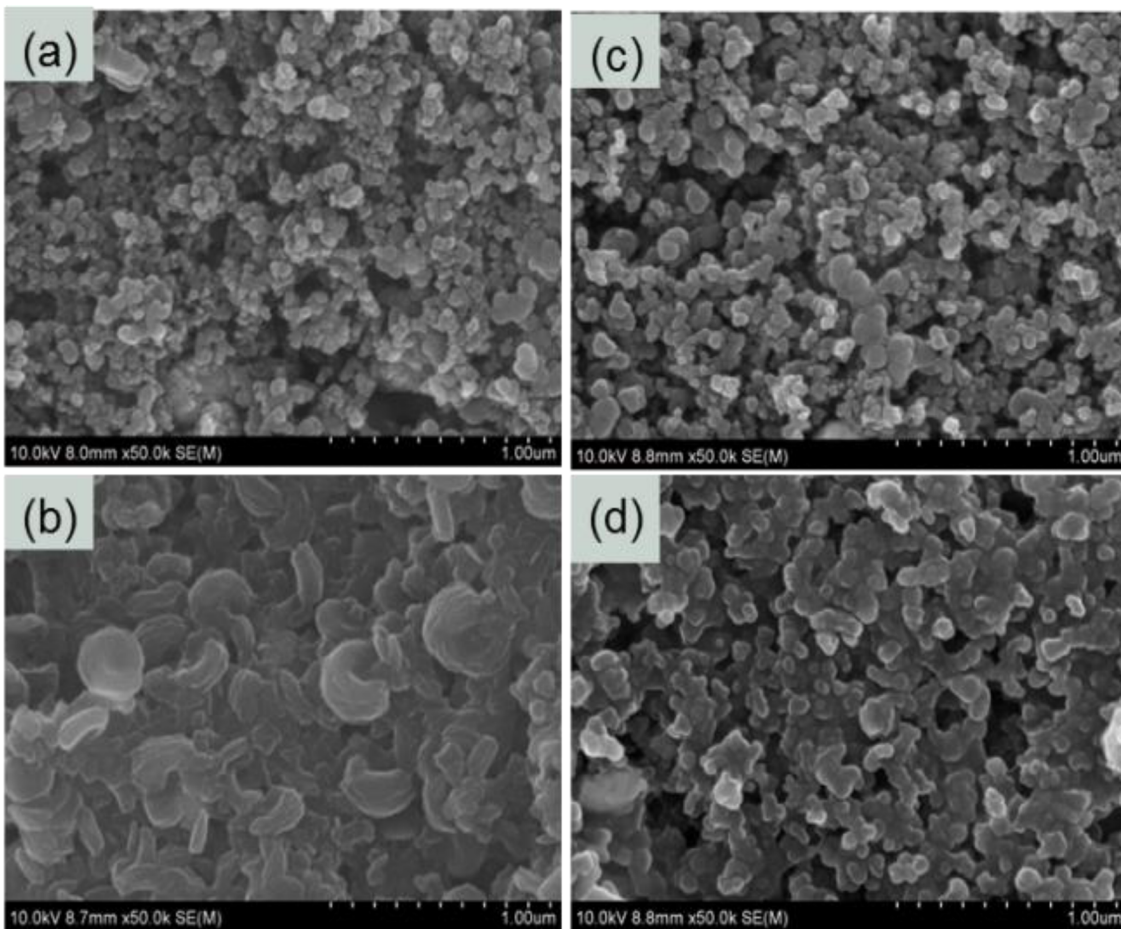


**Figure 8.** SEM images of the 3DOM-NFO-3/KB electrodes at different discharge–charge stages: initially (a), after the first discharge (b), after the first recharge (c), and after the 10th recharge (d) at a capacity restriction of 1000 mAh g<sub>C</sub><sup>-1</sup>.

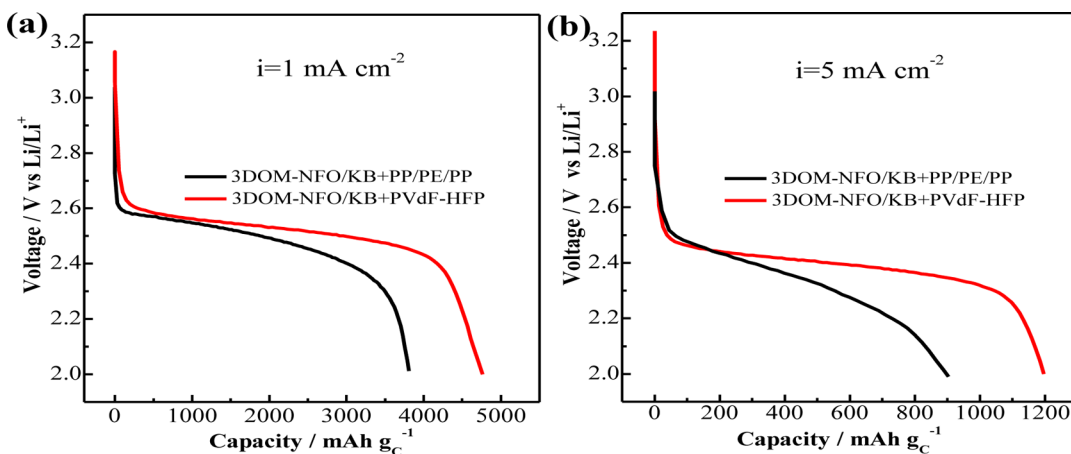


**Figure 9.** Discharge curves at (a) 1 and (b) 5 mA cm<sup>-2</sup> of Li–O<sub>2</sub> batteries equipped with the 3DOM-NFO-4/KB electrode, optimized PVdF-HFP membrane, and 1 M LiCF<sub>3</sub>SO<sub>3</sub>–TEGDME electrolyte.

is further improved to 4772 and 1215 mAh g<sub>C</sub><sup>-1</sup>, respectively, indicating an enhanced rate capability. This result further proves that the pore structure of the key material has a significant effect on the battery performance.

#### 4. CONCLUSION

3DOM NiFe<sub>2</sub>O<sub>4</sub> materials with tunable pore size were synthesized via a hard template as the bifunctional electrocatalyst for Li–O<sub>2</sub> batteries. The Li–O<sub>2</sub> battery using 3DOM

NiFe<sub>2</sub>O<sub>4</sub> as the electrocatalyst exhibits significantly enhanced rate capability, charge–discharge efficiency, and cyclability. Furthermore, enhanced battery performance is achieved with increasing pore size and pore volume. Such an improved performance can be ascribed to higher ORR and OER electrocatalytic activities, which are verified by the LSV results. The Li–O<sub>2</sub> battery employing 3DOM NiFe<sub>2</sub>O<sub>4</sub> with the largest pore size obtains a specific discharge capacity as high as 10830 mAh g<sub>C</sub><sup>-1</sup>, and an obviously improved cyclability of up to 100

cycles is observed when the capacity is restricted at 1000 mAh g<sub>C</sub><sup>-1</sup>. Moreover, employing a new separator such as the porous PVdF-HFP membrane further improves the rate capability of the Li—O<sub>2</sub> batteries. The investigation of materials with tunable pore structure indicates a promising way to design Li—O<sub>2</sub> batteries with high performance.

## AUTHOR INFORMATION

### Corresponding Authors

\*E-mail: yuant@sari.ac.cn. Tel. and Fax: +86-21-20321112.  
\*E-mail: yangh@sari.ac.cn. Tel. and Fax: +86-21-20321112.

### Notes

The authors declare no competing financial interest.

## ACKNOWLEDGMENTS

This work was supported by the National Basic Research Program of China (973 Program, Grant 2012CB932800), the National High-tech. 863 Program of China (Grant 2013AA050902), and the Shanghai Science and Technology Committee (Grant 11DZ1200400). X.L. is thankful for financial support from the Natural Science Foundation of Jiangsu Province (Grant BK2011272).

## REFERENCES

- (1) Chen, Y.; Freunberger, S. A.; Peng, Z.; Bardé, F.; Bruce, P. G. Li—O<sub>2</sub> Battery with a Dimethylformamide Electrolyte. *J. Am. Chem. Soc.* **2012**, *134*, 7952–7957.
- (2) Freunberger, S. A.; Chen, Y.; Drewett, N. E.; Hardwick, L. J.; Barde, F.; Bruce, P. G. The Lithium—Oxygen Battery with Ether-Based Electrolytes. *Angew. Chem., Int. Ed.* **2011**, *50*, 8609–8613.
- (3) Li, F.; Zhang, T.; Zhou, H. Challenges of Non-aqueous Li—O<sub>2</sub> Batteries: Electrolytes, Catalysts, and Anodes. *Energy Environ. Sci.* **2013**, *6*, 1125–1141.
- (4) Liang, C.; Wang, F.; Xu, Y.; Chen, J.; Liu, D.; Luo, Z. A Stable Electrolyte Makes a Nonaqueous Li—O<sub>2</sub> Battery Truly Rechargeable. *New J. Chem.* **2013**, *37*, 2568–2572.
- (5) Shao, Y.; Ding, F.; Xiao, J.; Zhang, J.; Xu, W.; Park, S.; Zhang, J.-G.; Wang, Y.; Liu, J. Making Li—Air Batteries Rechargeable: Material Challenges. *Adv. Funct. Mater.* **2013**, *23*, 987–1004.
- (6) Xu, W.; Xiao, J.; Wang, D.; Zhang, J.; Zhang, J.-G. Effects of Nonaqueous Electrolytes on the Performance of Lithium/Air Batteries. *J. Electrochem. Soc.* **2010**, *157*, A219–A224.
- (7) Ottakam Thotiyil, M. M.; Freunberger, S. A.; Peng, Z.; Bruce, P. G. The Carbon Electrode in Nonaqueous Li—O<sub>2</sub> cells. *J. Am. Chem. Soc.* **2013**, *135*, 494–500.
- (8) Cheng, F.; Chen, J. Metal—Air Batteries: from Oxygen Reduction Electrochemistry to Cathode Catalysts. *Chem. Soc. Rev.* **2012**, *41*, 2172–2192.
- (9) Christensen, J.; Albertus, P.; Sanchez-Carrera, R. S.; Lohmann, T.; Kozinsky, B.; Liedtke, R.; Ahmed, J.; Kojic, A. A Critical Review of Li/Air Batteries. *J. Electrochem. Soc.* **2012**, *159*, R1–R30.
- (10) Kraysberg, A.; Ein-Eli, Y. Review on Li-air batteries—Opportunities, Limitations and Perspective. *J. Power Sources* **2011**, *196*, 886–893.
- (11) Yang, X.-h.; He, P.; Xia, Y.-y. Preparation of Mesocellular Carbon Foam and its Application for Lithium/Oxygen Battery. *Electrochim. Commun.* **2009**, *11*, 1127–1130.
- (12) Guo, Z.; Zhou, D.; Dong, X.; Qiu, Z.; Wang, Y.; Xia, Y. Ordered Hierarchical Mesoporous/Macroporous Carbon: a High-Performance Catalyst for Rechargeable Li—O<sub>2</sub> Batteries. *Adv. Mater.* **2013**, *25*, S668–S672.
- (13) Park, J. B.; Lee, J.; Yoon, C. S.; Sun, Y. K. Ordered Mesoporous Carbon Electrodes for Li—O<sub>2</sub> Batteries. *ACS Appl. Mater. Interfaces* **2013**, *5*, 13426–13431.
- (14) Park, J.; Jun, Y.-S.; Lee, W.-r.; Gerbec, J. A.; See, K. A.; Stucky, G. D. Bimodal Mesoporous Titanium Nitride/Carbon Microfibers as Efficient and Stable Electrocatalysts for Li—O<sub>2</sub> Batteries. *Chem. Mater.* **2013**, *25*, 3779–3781.
- (15) Ryu, W.-H.; Yoon, T.-H.; Song, S. H.; Jeon, S.; Park, Y.-J.; Kim, I.-D. Bifunctional Composite Catalysts Using Co<sub>3</sub>O<sub>4</sub> Nanofibers Immobilized on Nonoxidized Graphene Nanoflakes for High-Capacity and Long-Cycle Li—O<sub>2</sub> Batteries. *Nano Lett.* **2013**, *13*, 4190–4197.
- (16) Yang, W.; Salim, J.; Ma, C.; Ma, Z.; Sun, C.; Li, J.; Chen, L.; Kim, Y. Flowerlike Co<sub>3</sub>O<sub>4</sub> Microspheres Loaded with Copper Nanoparticle as an Efficient Bifunctional Catalyst for Lithium—Air Batteries. *Electrochim. Commun.* **2013**, *28*, 13–16.
- (17) Zhang, L.; Zhang, S.; Zhang, K.; Xu, G.; He, X.; Dong, S.; Liu, Z.; Huang, C.; Gu, L.; Cui, G. Mesoporous NiCo<sub>2</sub>O<sub>4</sub> Nanoflakes as Electrocatalysts for Rechargeable Li—O<sub>2</sub> Batteries. *Chem. Commun.* **2013**, *49*, 3540–3542.
- (18) Xu, J. J.; Xu, D.; Wang, Z. L.; Wang, H. G.; Zhang, L. L.; Zhang, X. B. Synthesis of Perovskite-based Porous La<sub>0.75</sub>Sr<sub>0.25</sub>MnO<sub>3</sub> Nanotubes as a Highly Efficient Electrocatalyst for Rechargeable Lithium—Oxygen Batteries. *Angew. Chem., Int. Ed.* **2013**, *52*, 3887–3890.
- (19) Xu, J.-J.; Wang, Z.-L.; Xu, D.; Meng, F.-Z.; Zhang, X.-B. 3D Ordered Macroporous LaFeO<sub>3</sub> as Efficient Electrocatalyst for Li—O<sub>2</sub> Batteries with Enhanced Rate Capability and Cyclic Performance. *Energy Environ. Sci.* **2014**, *7*, 2213–2219.
- (20) Tran, C.; Yang, X.-Q.; Qu, D. Investigation of the Gas-Diffusion-Electrode Used as Lithium/Air Cathode in Non-Aqueous Electrolyte and the Importance of Carbon Material Porosity. *J. Power Sources* **2010**, *195*, 2057–2063.
- (21) Xiao, J.; Wang, D.; Xu, W.; Wang, D.; Williford, R. E.; Liu, J.; Zhang, J.-G. Optimization of Air Electrode for Li/Air Batteries. *J. Electrochim. Soc.* **2010**, *157*, A487–A492.
- (22) Wang, H.-W.; Hu, Z.-A.; Chang, Y.-Q.; Chen, Y.-L.; Wu, H.-Y.; Zhang, Z.-Y.; Yang, Y.-Y. Design and Synthesis of NiCo<sub>2</sub>O<sub>4</sub>-Reduced Graphene Oxide Composites for High Performance Supercapacitors. *J. Mater. Chem.* **2011**, *21*, 10504–10511.
- (23) Wang, Z.; Zhang, X.; Li, Y.; Liu, Z.; Hao, Z. Synthesis of Graphene—NiFe<sub>2</sub>O<sub>4</sub> Nanocomposites and Their Electrochemical Capacitive Behavior. *J. Mater. Chem. A* **2013**, *1*, 6393–6399.
- (24) Yuan, C.; Li, J.; Hou, L.; Zhang, X.; Shen, L.; Lou, X. W. Ultrathin Mesoporous NiCo<sub>2</sub>O<sub>4</sub> Nanosheets Supported on Ni Foam as Advanced Electrodes for Supercapacitors. *Adv. Funct. Mater.* **2012**, *22*, 4592–4597.
- (25) Lee, Y. I.; Jang, D. H.; Kim, J. W.; Kim, W. B.; Choa, Y. H. Electrospun NiFe<sub>2</sub>O<sub>4</sub> Nanofibers as High Capacity Anode Materials for Li-Ion Batteries. *J. Nanosci. Nanotechnol.* **2013**, *13*, 7138–7141.
- (26) Lavela, P.; Kyeremateng, N. A.; Tirado, J. L. NiMn<sub>2-x</sub>Fe<sub>x</sub>O<sub>4</sub> Prepared by a Reverse Micelles Method as Conversion Anode Materials for Li-Ion Batteries. *Mater. Chem. Phys.* **2010**, *124*, 102–108.
- (27) Li, J.; Xiong, S.; Liu, Y.; Ju, Z.; Qian, Y. High Electrochemical Performance of Monodisperse NiCo<sub>2</sub>O<sub>4</sub> Mesoporous Microspheres as an Anode Material for Li-Ion Batteries. *ACS Appl. Mater. Interfaces* **2013**, *5*, 981–988.
- (28) Wang, H.; Yang, Y.; Liang, Y.; Zheng, G.; Li, Y.; Cui, Y.; Dai, H. Rechargeable Li—O<sub>2</sub> Batteries with a Covalently Coupled MnCo<sub>2</sub>O<sub>4</sub>—Graphene Hybrid as an Oxygen Cathode Catalyst. *Energy Environ. Sci.* **2012**, *5*, 7931–7935.
- (29) Prabu, M.; Ketpang, K.; Shanmugam, S. Hierarchical Nanostructured NiCo<sub>2</sub>O<sub>4</sub> as an Efficient Bifunctional Non-precious Metal Catalyst for Rechargeable Zinc—Air Batteries. *Nanoscale* **2014**, *6*, 3173–3181.
- (30) Li, J.; Zou, M.; Wen, W.; Zhao, Y.; Lin, Y.; Chen, L.; Lai, H.; Guan, L.; Huang, Z. Spinel MFe<sub>2</sub>O<sub>4</sub> (M = Co, Ni) Nanoparticles Coated on Multi-Walled Carbon Nanotubes as Electrocatalysts for Li—O<sub>2</sub> Batteries. *J. Mater. Chem. A* **2014**, *2*, 10257–10262.
- (31) Hong, D.; Yamada, Y.; Nagatomi, T.; Takai, Y.; Fukuzumi, S. Catalysis of Nickel Ferrite for Photocatalytic Water Oxidation Using [Ru(bpy)<sub>3</sub>]<sup>2+</sup> and S<sub>2</sub>O<sub>8</sub><sup>2-</sup>. *J. Am. Chem. Soc.* **2012**, *134*, 19572–19575.
- (32) Hu, W.; Qin, N.; Wu, G.; Lin, Y.; Li, S.; Bao, D. Opportunity of Spinel Ferrite Materials in Nonvolatile Memory Device Applications Based on Their Resistive Switching Performances. *J. Am. Chem. Soc.* **2012**, *134*, 14658–14661.

- (33) Li, L.; Li, G.; Smith, R. L.; Inomata, H. Microstructural Evolution and Magnetic Properties of  $\text{NiFe}_2\text{O}_4$  Nanocrystals Dispersed in Amorphous Silica. *Chem. Mater.* **2000**, *12*, 3705–3714.
- (34) Li, Y.; Yin, Y.; Guo, K.; Xue, X.; Zou, Z.; Li, X.; He, T.; Yang, H. Tuning Pore Structure of the Poly(vinylidene Difluoride Hexafluoropropylene) Membrane for Improvement in Rate Performance of Li–Oxygen Battery. *J. Power Sources* **2013**, *241*, 288–294.
- (35) Yang, H.; Shi, Q.; Tian, B.; Lu, Q.; Gao, F.; Xie, S.; Fan, J.; Yu, C.; Tu, B.; Zhao, D. One-Step Nanocasting Synthesis of Highly Ordered Single Crystalline Indium Oxide Nanowire Arrays from Mesostructured Frameworks. *J. Am. Chem. Soc.* **2003**, *125*, 4724–4725.
- (36) Ren, Y.; Ma, Z.; Bruce, P. G. Ordered Mesoporous Metal Oxides: Synthesis and Applications. *Chem. Soc. Rev.* **2012**, *41*, 4909–4927.
- (37) Jiao, F.; Hill, A. H.; Harrison, A.; Berko, A.; Chadwick, A. V.; Bruce, P. G. Synthesis of Ordered Mesoporous NiO with Crystalline Walls and a Bimodal Pore Size Distribution. *J. Am. Chem. Soc.* **2008**, *130*, 5262–5266.
- (38) Li, Y.; Zou, L.; Li, J.; Guo, K.; Dong, X.; Li, X.; Xue, X.; Zhang, H.; Yang, H. Synthesis of Ordered Mesoporous  $\text{NiCo}_2\text{O}_4$  via Hard Template and its Application as Bifunctional Electrocatalyst for Li– $\text{O}_2$  Batteries. *Electrochim. Acta* **2014**, *129*, 14–20.
- (39) Adams, B. D.; Radtke, C.; Black, R.; Trudeau, M. L.; Zaghib, K.; Nazar, L. F. Current Density Dependence of Peroxide Formation in the Li– $\text{O}_2$  Battery and its Effect on Charge. *Energy Environ. Sci.* **2013**, *6*, 1772–1778.
- (40) Lu, Y. C.; Crumlin, E. J.; Veith, G. M.; Harding, J. R.; Mutoro, E.; Baggetto, L.; Dudney, N. J.; Liu, Z.; Shao-Horn, Y. In Situ Ambient Pressure X-ray Photoelectron Spectroscopy Studies of Lithium–Oxygen Redox Reactions. *Sci. Rep.* **2012**, *2*, 715–720.
- (41) Lu, Y.-C.; Gasteiger, H. A.; Parent, M. C.; Chiloyan, V.; Shao-Horn, Y. The Influence of Catalysts on Discharge and Charge Voltages of Rechargeable Li–Oxygen Batteries. *Electrochim. Solid-State Lett.* **2010**, *13*, A69–A72.